Experimental Thermal and Fluid Science 178 (2026) 111820

Contents lists available at ScienceDirect

Experimental Thermal and Fluid Science

journal homepage: www.elsevier.com/locate/etfs

Enhanced momentum dissipation in bubble column reactors: design and experimental analysis of swirl flow optimization☆

Ahmad Salam Farooqi [a,b,*], Khairuddin Sanaullah [c], Mohamed A. Kotb [d], Nicholas J. Watson [e], Atia E. Khalifa [d,f], Shahid Rasul [a], Medhat A. Nemitallah [g,h]

[a] Faculty of Science and Environment, Northumbria University, Newcastle Upon Tyne NE1 8ST, UK
[b] Department of Chemical Engineering and Energy Sustainability, Faculty of Engineering, Universiti Malaysia Sarawak, 94300 Kota Samarahan, Sarawak, Malaysia
[c] Discipline of Chemical Engineering, School of Engineering, College of Agriculture, Engineering & Science, Howard Campus, University of KwaZulu-Natal, Glenwood, Durban, South Africa
[d] Mechanical Engineering Department, King Fahd University of Petroleum & Minerals, Dhahran 31261, Saudi Arabia
[e] School of Food Science and Nutrition, University of Leeds, Leeds LS2 9JT, UK
[f] Interdisciplinary Research Center for Sustainable Energy Systems, King Fahd University of Petroleum & Minerals, Dhahran 31261, Saudi Arabia
[g] Aerospace Engineering Department, King Fahd University of Petroleum & Minerals, Dhahran 31261, Saudi Arabia
[h] Interdisciplinary Research Center for Hydrogen Technologies and Carbon Management, King Fahd University of Petroleum & Minerals, Dhahran, 31261, Saudi Arabia

ARTICLE INFO

Keywords:
Bubble column reactor
Swirl-injection flow
Momentum dissipation
Particle image velocimetry
Gas-liquid two-phase flow

ABSTRACT

This study develops a new momentum-dissipation system for bubble column reactors (BCRs). The operation of BCRs primarily depends on various two-phase flow factors, including geometric configurations (e.g., gas injection), operational conditions (e.g., temperature, pressure, and liquid and gas flow rates), and gas–liquid mass transfer. Among these, the bubble injection geometry plays a particularly important role, influencing parameters such as the gas void fraction and interfacial area. In this study, a bubbly flow rig was built, primarily featuring a bubble-injection mechanism that induces swirl in gas–liquid bubbly flows. Different open-channel configurations were designed to dissipate momentum, which is essential for reducing the liquid's rotary motion while promoting bubble swirl within the static liquid. This allows for measurement of the liquid-phase velocity field and a qualitative assessment of bubble–liquid slip behavior. PIV technique was applied to single and two-phase systems in a laboratory setting with water and air serving as the working fluids. The experiments assessed the impact of four fins with different geometries, including simple holes and open channels, on velocity vectors across the horizontal plane and, consequently, on liquid momentum. Velocity fields with swirl gas injection were also compared to those without air injection to evaluate the behavior of interacting fluids. Results show that both 90° and 180° open channels produce significantly greater momentum dissipation than the straight and simple hole configurations, with the 90° open channel achieves the highest dissipation overall. Two-plane PIV was used to experimentally map the hydrodynamics of a swirl-injection bubble column reactor equipped with a collar with fins, providing new insight and design guidance for swirl-driven multiphase reactors.

1. Introduction

Injecting gas bubbles through a column of liquid is a technique used in various industrial processes, such as oil and gas production, chemical and biochemical industries, and many others [1–3]. These bubble column reactors (BCRs) are usually cylindrical, with a gas distribution system at the bottom, also known as a sparger. The gas is introduced into the liquid phase through the sparger as bubbles [2]. This discrete nature of bubbles gives rise to complex interphase interaction in bubble columns. In addition to hydrodynamics, mass transfer between the gas and liquid phases is a key parameter that determines the process efficiency. However, the mass transfer relies heavily on the column hydrodynamics, including liquid shear, gas void fraction, bubble properties (i.e., shape, size, velocity, etc.), and physical properties of gas and liquid phases [4–8].

Many experimental investigations have studied the effects of various

☆ This article is part of a special issue entitled: 'Cavitation & Bubbles' published in Experimental Thermal and Fluid Science.

* Corresponding author at: Faculty of Science and Environment, Northumbria University, Newcastle Upon Tyne NE1 8ST, UK.
E-mail address: ahmad.farooqi@northumbria.ac.uk (A.S. Farooqi).

https://doi.org/10.1016/j.expthermflusci.2026.111820
Received 12 October 2025; Received in revised form 5 August 2026; Accepted 9 August 2026
Available online 10 August 2026
0894-1777/

parameters on the operation of a BCRs [9–11]. The factors influencing column operations include the design of gas distributor plates; the geometry of the column and its internals; operating pressure and temperature; the addition of tertiary components such as alcohols; and the physical properties and superficial velocities of the gas and liquid phases. The effect of sparger design has attracted large research attention due to its role in defining the bubble column hydrodynamics [12–14]. Sparger geometry determines the shape and velocity of the bubbles entering the column. Well-known gas spargers include porous and perforated plates, membrane and ring-type distributors, among others [2]. The most commonly used plate types are the sieve plate and the porous plate [15]. Although porous plates provide a uniformly distributed bubble size, they can cause a higher pressure drop compared to a sieved plate. On the other hand, sieve plate sparger can cause gas jetting into the liquid, which is undesireable as it produces non-uniform gas distribution.

The porous sparger offers an enhanced gas-liquid contact area for improved heat and mass transfer, owing to the formation of a large number of small bubbles [16]. The geometry of the gas sparger and the hole size of the porous plate affect the bubble characteristics (i.e., shape, size, and velocity), which influence the mean gas void fraction. The gas void fraction is defined as the ratio of gas volume to the total volume of the gas-liquid mixture. Unless stated otherwise, void fraction here refers to a time-and cross-sectionally averaged quantity, following common bubble column reactor practice. Luo et al. [17] reported that the void fraction was influenced by the type of gas sparger employed in the bubble column. Schumpe and Grund [18] worked with various gas distributors, including perforated plates and ring-type gas spargers. They found that a ring-type gas sparger produced a lower gas void fraction than a perforated plate, and that, for the ring sparger, the void fraction increased gradually with rising gas superficial velocity.

Momentum dissipation refers to the loss of momentum in fluid flow due to internal factors such as viscosity or external forces, resulting in the conversion of kinetic energy into heat or other forms of energy. It is essential for understanding energy losses in turbulent flows and is described by the Navier-Stokes equations. Swirl flow, meanwhile, involves the rotational motion of fluid around an axis, creating a vortex-like pattern. This phenomenon is often used in engineering applications, such as combustion chambers and pipelines, to improve mixing and flow stability. Both concepts are vital for managing fluid dynamics in complex systems. Li et al. [19] investigated the optimization of circular gas distributor configurations in slurry bubble column reactors using a Computational Fluid Dynamics–Population Balance Model (CFD-PBM) coupled model. The study found that increasing the distributor's opening size and ring diameter improved gas holdup, bubble uniformity, and liquid circulation. This enhancement improved momentum transfer and reactor performance. The optimal setup features a distributor with a 10 mm opening diameter and a 0.20 m ring diameter, offering reliable guidance for scale-up synthesis processes [19]. Abdulrahman et al. [20] employed two-dimensional CFD simulations with an Eulerian-Eulerian approach and k–ε turbulence modeling to predict gas holdup in helium-water-alumina slurry bubble columns under different conditions of gas velocity, liquid height, and solid concentration. The study showed that gas holdup increased with gas velocity but decreased with higher liquid heights and solid concentrations, with a maxmimum deviation of 28.5% from experimental data. These findings demonstrate the CFD model's usefulness for hydrodynamic analysis and scaling up multiphase reactors.

Swirl flow is among the established methods to intensify certain industrial processes, with the added advantage of enhanced mass transfer [19]. Swirl flow has been used in technology involving pneumatic conveying to lessen the pressure drop, which results in lowering the required power to drive the flow [20]. Swirl flow is also applied in nuclear fuel assemblies to enhance heat transfer [21]. Similarly, the - swirling motion of solid particles has been used to enhance the thermal hydraulics of fluidized beds [22]. Due to these advantages, there has been a great deal of interest shown by the scientific and academic community to understand and optimize the use of controlled swirl flows in single-phase flow-based applications[21,23].

In recent years, there has been a significant increase in the use of swirl motion in multiphase flow operations [24–27]. Cazan and Aidun [25] used Laser Doppler Velocimetry (LDV) to measure the liquid velocity of circular pipe flow and a charge-coupled device (CCD) camera to visualize the air bubbles. Hamdani et al. [20] experimentally investigated the swirl bubbly flow among air and water moving co-currently and revealed that swirl injection of bubbly flow influenced the bubble distribution, which subsequently increased the gas void fraction. Sivaiah et al. [28] emphasized mass transfer across the bubble-liquid interface as the key parameter. Whereas Shanmugam et al. [29] reported that swirl bubbly flow can maintain axial and radial bubble dispersion, thereby increasing the void fraction as smaller bubbles coalesce into larger ones. Lucas and Mishra [30] measured the localized velocity components of gas (i.e., axial, radial, and azimuthal) in gas–liquid bubbly flow with a novel conductance wire. Wang et al. [31] utilized Electrical Resistance Tomography (ERT) to measure local air void fraction and velocity distribution in gas–liquid flows. Radial voidage distribution, bubble velocity, bubble size, bubble frequency, and interfacial area concentration were measured using a local dual-optical probe in an air–water, bubbly, upward flow by Shoukri et al. [32].

Experimental techniques used for multiphase flow investigations are commonly classified as intrusive or non-intrusive. Intrusive techniques require the physical insertion of probes or sensors into the flow field, potentially disturbing the local hydrodynamics. Non-intrusive techniques, such as Particle Image Velocimetry (PIV), rely on optical access and external measurements. Although PIV requires the introduction of tracer particles, these particles are selected to be sufficiently small and neutrally buoyant so that they faithfully follow the flow without significantly disturbing it; therefore, PIV is generally considered a non-intrusive measurement technique [33–35]. PIV is an excellent technique to study flows and turbulent structures. A significant advancement came with the introduction of cross-correlation of double images for velocity measurements [36]. PIV measurements in bubbly flow require several refinements, including phase separation and masking, optimal tracer selection, appropriate illumination and advanced multi-phase PIV methods. These refinements are crucial to overcoming challenges like optical distortions, reflections, and bubble-induced disturbances, enabling accurate measurement of the liquid-phase velocity field in bubbly flows.

Since the development of PIV, many researchers have used the technique to study bubbly flow in gas–liquid reactors. PIV has been applied to bubbly flows, pioneered by Oakley [37], who employed a cinematic PIV to solve for the liquid flow field and a tracking technique to resolve the motion of individual gas bubbles. Delnoij et al. [38] examined the gas and liquid flow fields induced by a bubble plume rising in a rectangular bubble column. Pereira et al. [39] investigated a three-dimensional imaging system for mapping two-phase bubbly flows. An ensemble correlation approach for bubbly flow based on the single-frame double-exposure technique with image shifting was developed to overcome directional ambiguity, in which about 10–15 images were ensemble-averaged prior to PIV processing to identify the two correlation peaks for bubbles and liquid [40]. Liu and Zheng [41] used PIV to investigate changes in bubble trajectories and shape as a function of liquid viscosity, and observed vortices, crossflow, and circular motion caused by the bubbles within the column. PIV is a powerful tool for investigating multiphase flow, enabling one to understand complex phenomena by determining the velocities of the continuous and dispersed phases [42]. PIV supported by a monochromatic, coherent laser and a CCD camera, can image bubbles as small as 4 mm [43]. It provides planar imaging velocimetry, which has been found useful in exhibiting the hydrodynamics of bubbly flows. The use of PIV in an air–water two-phase system has emerged as a reliable technique for studying turbulence in gas–liquid flows with relatively high void fractions [8]. PIV has been used on a vertical pipe, and image pre- and post-processing techniques have been adapted to determine the drift velocity, void fraction, and vorticity fields in the liquid phase [44]. Demong et al. [45] generated the swirl bubble flow using a rotating sparger. They investigated the impact of swirl flow on the hydrodynamics of gas–liquid bubbly flow reactors using CFD simulations, and found that the gas void fraction and shear stress increased with increasing gas rate. Swirl flow was also found to enhance mixing efficiency by generating eddies, thereby increasing mass transfer and reactor performance. The results suggested that swirl-induced bubbles and flow patterns could significantly improve reactor design and operation efficiency.

Despite extensive research on bubble column reactors, experimental studies of swirl-injection systems remain limited, particularly with regard to the role of internal geometries in controlling liquid momentum and swirl propagation. Furthermore, there is a lack of systematic experimental comparison of different fin and channel configurations using quantitative flow diagnostics such as PIV. To address this gap, the present study experimentally investigates the hydrodynamics of a swirl-injection bubble column reactor equipped with a novel finned collar designed for momentum-dissipation. Two-plane PIV is employed to map the liquid-phase velocity fields both inside the collar and 5 cm above it, under single- and two-phase conditions. Four different fin geometries (simple holes, straight channels, and open channels with 90° and 180° bends) are compared to evaluate their effectiveness in dissipating liquid momentum and controlling swirl flow. Rigorous experimental procedures, including optical distortion correction, phase masking, and statistical convergence analysis are used to ensure reliable velocity measurements with negligible tracer slip. The findings clarify the influence of fin geometry on momentum dissipation and provide practical design guidance for optimizing hydrodynamics, bubble–liquid interaction, and energy efficiency in swirl-driven multiphase reactors.

2. Equipment and methods

2.1. Experimental setup

The experimental setup, shown in Fig. 1, consists of a cylindrical Perspex column (thickness 0.5 cm, height 61 cm and inner diameter 59 cm), a perforated sparger (diameter 7 cm. hole diameter 1 mm), and a collar (height 11.5 cm, inner diameter 20 cm) fitted with fins containing open channels. The fins serve as internals to dissipate the liquid momentum caused by the rotation of the sparger. Without internal fittings, the fluid motion follows the sparger's rotation producing organized, periodic flow patterns; in configurations with fins, these organized patterns remain visible but are further shaped by the internal channels and bends. In this study, planar PIV was used to measure and analyze the liquid-phase velocity field in the bubble column reactor, providing insight into how different fin geometries affect liquid momentum dissipation, swirl flow dynamics, and bubble slip conditions. By capturing velocity vectors across various fin configurations, the PIV data support conclusions on the optimal fin designs for enhancing hydrodynamics in swirl-injection reactors. Gas was injected into a stagnant liquid at three sparger rotating speeds: 30, 90, and 150 rpm. Tap water at room temperature and air were used as the liquid and gas phases, respectively. The column was filled with water to a height of 50 cm. Air was supplied by an oil-free industrial air compressor with a maximum working pressure of 8 bar; detailed manufacturer information for this unit is no longer available to the authors, but its operating conditions during the experiments are fully reported to allow reproduction on equivalent equipment. The gas flow rate was measured using a thermal mass flow meter with a stated accuracy of ± 1.5% of full scale over the operating range of 15–25 °C and 34–414 kPa. The sparger rotation was driven by a variable-speed DC motor coupled to the sparger shaft via a belt drive, with the rotational speed set and monitored using a calibrated motor controller. A semi-rectangular box filled with the same working fluid (water) was positioned around the vertical column to minimize optical distortion caused by the column's curvature; the box was made of Perspex, matching the main column.

Different channel configurations were tested, including simple holes,

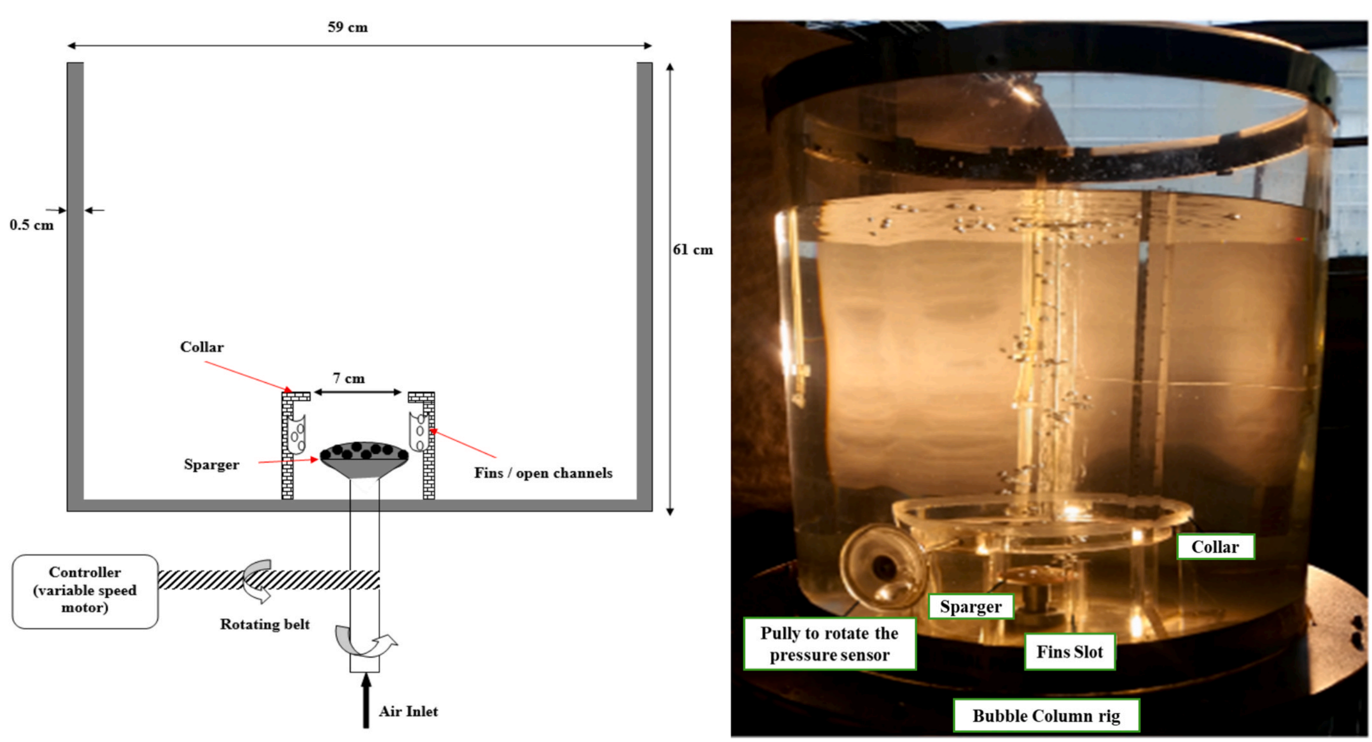

Fig. 1. Schematic diagram and photographic view of the experimental bubble column reactor (BCR) setup.

straight channels, 90° bends, and 180° bends, all mounted within the collar surrounding the air sparger, as shown in Fig. 2. The fins were fabricated from Plexiglass, which provides transparency for flow visualization and is lightweight and easy to manipulate for experimental setups. The first configuration (Fig. 2**a**) features simple circular holes, allowing straightforward flow through the fins with minimal interference. The second design (Fig. 2**b**) incorporate straight channels aligned with the flow, intended to guide the fluid smoothly through the conical fins, potentially reducing turbulence and improving flow efficiency. In the third configuration (Fig. 2**c**), the channels incorporate a 90° bend, which may introduce swirl and enhance mixing by redirecting the flow, increasing surface contact, and potentially improving heat transfer. Finally, the fourth design (Fig. 2**d**) features 180° curved channels, creating a strong flow redirection expected to generate significant swirl, increase residence time, and introduce turbulence, further enhancing mixing.

2.2. Measurement technique

PIV was used to measure the velocity field of the liquid phase (Fig. 3). Of the two horizontal measurement planes (see Fig. 4), Plane 1 is located inside the collar at 8 cm from the column base (approximately mid-height of the 11.5 cm collar), while Plane 2 is located 5 cm above the collar top edge. These planes were chosen to examine the velocity fields for the following cases: no fins in place, simple hole, straight open channel, open channel with 90° and 180° bends. Bubble identification was achieved using a combination of cross-correlation techniques and post-processing filters to remove spurious vectors. Tracer particles were carefully selected to track the liquid phase and to minimze the interference from bubbles. In the two-phase experiments, PIV analysis was restricted to the liquid phase: bubbles were masked and excluded during cross-correlation processing, ensuring they did not distort the liquid-phase velocity measurements. Consequently, bubble velocities and explicit slip velocities ($u_b - u_\ell$) were not directly measured.

The water was seeded with hollow glass tracer particles with a refractive index of 1.52, mean diameter of 10 µm and a density of 1.1 g/cm^3. The dynamic viscosity of water at room temperature is approximately 0.001 Pa.s. For the Stokes number calculation, the characteristic length scale was taken as the inner diameter of the collar (0.2 m). The maximum and minimum flow velocities were 0.18 m/s and 0.01 m/s, respectively. The resulting Stokes numbers were 1.38×10^{-5} at the maximum velocity and 7.64×10^{-7} at the minimum velocity. These low values indicate that the seeding particles effectively follow the flow, ensuring accurate PIV measurements in the liquid phase.

The flow field was illuminated by two consecutive pulsed laser exposures separated by a known time interval, capturing images of slightly displaced tracer particles. PIV measurements were performed using a Dantec Dynamics PIV system. Illumination was provided by a double-pulsed Nd:YAG laser operating at a wavelength of 532 nm, with a maximum pulse energy of 500 mJ over 5 ns and a repetition rate of 15 Hz. The laser sheet defined a horizontal observation plane that intersected two consecutive open channels, the collar wall, and the adjacent region of the column. The pixel resolution corresponded to 0.12 mm per pixel, and the inter-frame time separation (Δt) between the double-pulsed laser exposures was 750 µs. Successive images of the flow were captured using a FlowSense 2M (Dantec Dynamics) CCD camera with 1600 × 1200 pixel resolution and 8-bit digital output, operating in double frame mode. Fifty double-frame image pairs were recorded for each condition. PIV processing was performed using Dantec Dynamic Studio software and involved pre-treatment, vector computation, and post-treatment. All instruments used were standard laboratory-grade equipment, and key operating parameters are reported above to allow reproduction of the experiments.

In PIV measurements, the number of image pairs required for statistical convergence depends on the flow conditions and measurement objectives. For time-averaged velocity fields in turbulent and swirling flows, ensemble sizes of several tens of image pairs are commonly used to obtain statistically converged mean fields [33–37]. In the present study, 50 double-framed image pairs were used, which were found to be sufficient to obtain stable mean velocity fields. The analysis consists of three stages. The first stage is pre-processing, in which masking is applied to remove unwanted regions from the raw image as shown in Fig. 5**a and 5b**. The second stage is vector computation by cross-correlation, performed on the ensemble of particle displacements

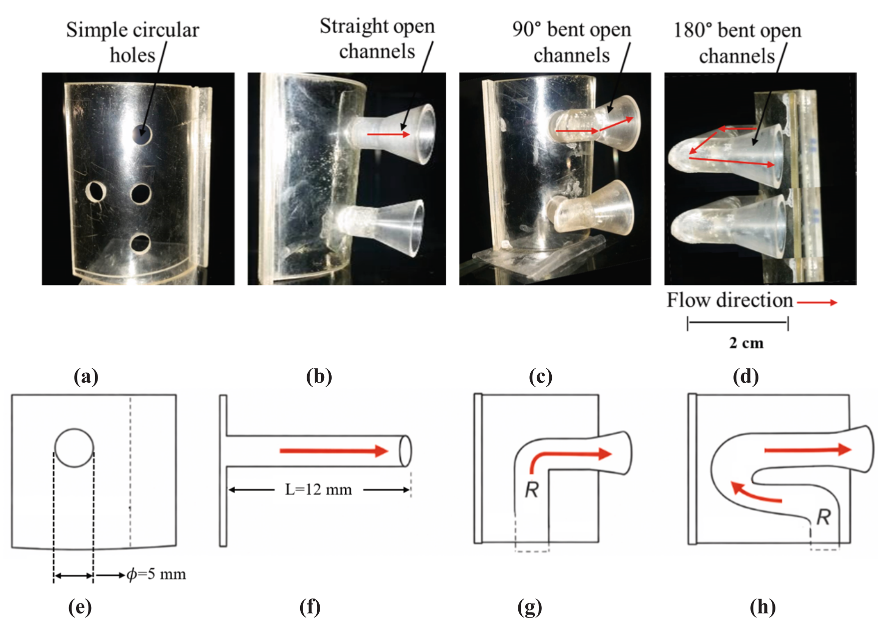

Fig. 2. Comparison of fin and channel geometries used for momentum dissipation: (a–d) photographic views and (e–h) corresponding schematic representations of the different configurations, including simple circular holes, straight open channels, 90° bent open channels, and 180° bent open channels. Red arrows indicate the primary flow direction through each geometry. The schematics identify the principal geometric parameters, where ϕ denotes the hole diameter, L the straight channel length, and R the bend radius. The nominal dimensions used for the schematic representations are ϕ = 5 mm, L = 12 mm, R = 5 mm for the 90° open channel, and R = 15 mm for the 180° open channel. A 2 cm scale bar is provided for the photographic images.

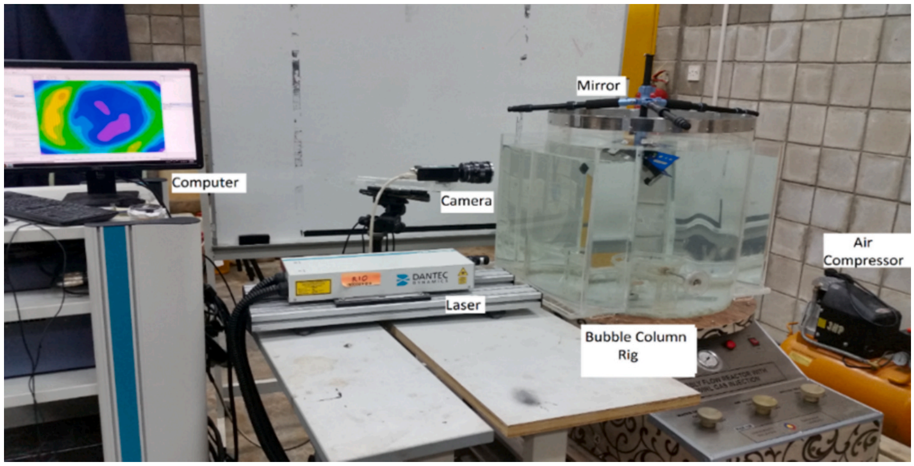

Fig. 3. Photographic view of the PIV experimental setup.

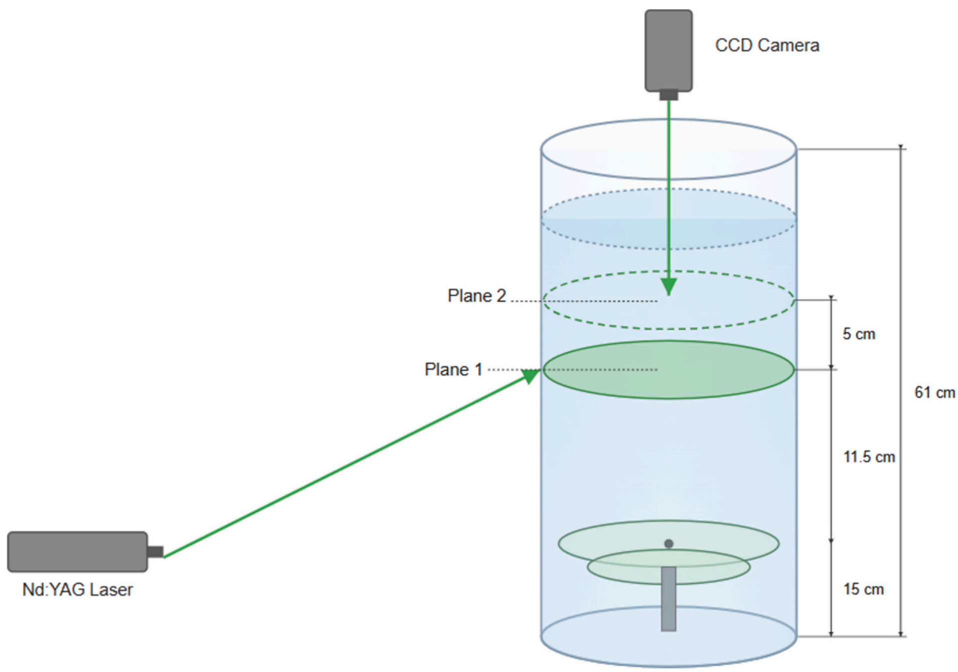

Fig. 4. Schematic of the PIV measurement arrangement (not to scale). The Nd:YAG laser generated a thin horizontal laser sheet that was positioned at either Plane 1 or Plane 2 during separate experiments, while the CCD camera was aligned normal to the illuminated plane to record the liquid-phase velocity field. Plane 1 was located inside the collar at a height of 15 cm from the column base, whereas Plane 2 was located 5 cm above the collar.

within each interrogation region (IR) of the masked image; the size of the IR is chosen based on the object space and the expected particle displacement. In the present study, cross-correlation with a 50% overlap and a fixed IR of 64 × 64 pixels was used, as depicted in Fig. 5**c.** The interrogation window size is comparable to smaller than the largest bubbles observed, although some spatial averaging remains inevitable in regions with smaller bubbles. The 50% overlap improves spatial resolution, and careful post-processing removes spurious vectors to improve the accuracy of the final velocity field. The final stage is post-processing, in which spurious vectors, identifiable by their direction or magnitude differing markedly from those of neighbouring vectors are removed as shown in Fig. 5**c.** The first step in post-processing is a moving average validation, which accepts or rejects outlier vectors by comparison with their neighbours, as illustrated in Fig. 5**d.** A rectangular neighborhood of $m \times n$ vectors is defined on the vector grid (a 5 × 5 window is used here), and then the moving average of all vectors within this neighbourhood is compared with each vector at its centre. The averaging formula is given by:

$$\overline{U}(x,y) = \frac{1}{mn}\sum_{i=x-\frac{n-1}{2}}^{x+\frac{n-1}{2}}\sum_{j=x-\frac{n-1}{2}}^{x+\frac{n-1}{2}} U(i,j) \tag{1}$$

where U is the velocity and $\overline{U}$ is the average velocity in the $m \times n$ neighborhood. The vectors are compared with the above average and are rejected if,

$$|U(x,y) - \overline{U}(x,y)| > K \tag{2}$$

where K is a number defined by,

$$K = \varepsilon \max_{x,y}|U(x,y) - \overline{U}(x,y)| \tag{3}$$

where ε is an acceptance factor, $0 < \varepsilon < 1$. The second post-processing stage is average filtering. Small scale velocity fluctuations within each

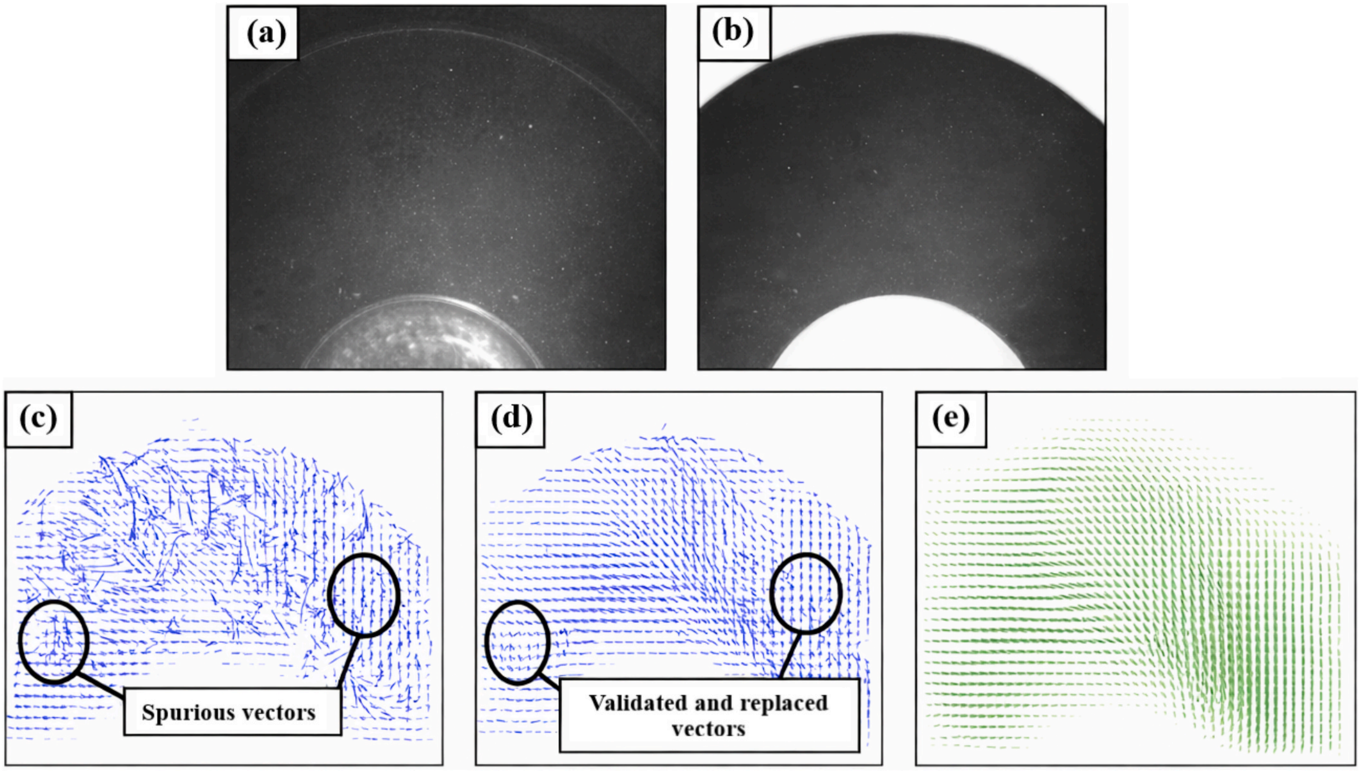

Fig. 5. PIV image processing steps: (a) raw image, (b) masked image, (c) initial cross-correlation vector field containing spurious vectors, (d) validated vector field after moving-average validation, and (e) final velocity field after additional filtering.

interrogation area are treated as noise, and filtering reduces this noise particularly important for downstream calculations involving derivatives such as vorticity. Each vector is replaced by the uniformly weighted average of its m × n neighborhood Equation (3). Fig. 5**e** shows the vector field after moving average filtering.

The authors acknowledge that the current experimental setup has certain limitations, such as resolution constraints and hardware restrictions, which prevent more advanced measurements such as time-resolved PIV or detailed turbulence analysis. While some spurious vectors were observed in Fig. 5**c** due to seeding non-uniformity and optical challenges, these were addressed through improved post-processing techniques and adjustments, as shown in Fig. 5**d and 5e**, ensuring the reliability of the velocity field measurements.

3. Results and discussion

In this section, the velocity fields of the water inside and outside the collar obtained by PIV are presented. It should be noted that all reported velocity fields correspond to the liquid phase only, as the PIV setup was configured to measure the motion of the continuous liquid phase with the bubble images masked. As stated above, the purpose of these measurements is to examine the influence of the four fins of different geometries on the velocity profiles compared with the case of no fin in place. Dissipating the liquid momentum in the reactor offers several benefits that enhance its overall efficiency and performance. Excess liquid momentum, generated by the sparger's rotation, can disrupt the bubble slip velocity, which is a critical factor for effective mass transfer. By reducing this excess momentum, the reactor achieves a controlled hydrodynamic environment that promotes uniform bubble distribution and stabilizes the flow. This improved stability enhances gas–liquid interaction, which is crucial for efficient heat and mass transfer processes, ultimately supporting applications like effluent treatment and biofuel production. In summary, momentum dissipation reduces energy losses, ensures operational stability, and optimizes reactor performance. Swirl flow is essential because it creates a highly dynamic flow regime that improves gas dispersion, enhances bubble breakup and phase interaction, and increases void fraction and interfacial area. While the resulting momentum is partially dissipated, the swirl motion introduces eddies and vortices that enhance mixing and interphase mass transfer. The momentum dissipation system is not intended to eliminate the benefits of swirl flow but to control the excess energy that could lead to uneven mixing or hinder bubble slip. This balance allows the reactor to exploit the advantages of swirl flow while mitigating its drawbacks, such as excessive turbulence or inefficient energy use. Furthermore, the velocity fields with and without swirl gas injection are also compared to characterize the interaction between the two phases.

3.1. Swirl flow BCR without air injection

In this case, there is no air injection and the system contains a single phase only, i.e., water. Fig. 6 shows the velocity field for the liquid at different sparger rotation speeds without air injection. This figure represents the influence of four different fins geometries(shown pictorially in Fig. 2 above) on the velocity plots. On comparing the velocity plots obtained for each of the four internals with that for the case of no fin in place, a marked reduction in the magnitude of velocity vectors is clearly visible for all four fins configurations. However, the maximum reduction in velocity occurs for the fin with a 90° open channel, corresponding to the highest momentum dissipation. A detailed discussion of the fins and their influence on the dissipation of liquid momentum generated at various sparger rotation speeds is presented in the following sub-section.

(a) Inside the collar

Three sparger rotation speeds i.e., 30, 90, and 150 rpm, were applied to examine the extent to which the different open channel geometries dissipate the liquid momentum generated by the sparger’s rotation. As the rotation speed increased, the velocity of the surrounding fluid also increased due to the higher momentum transferred to it. Fig. 6 **(a, f, and k)** shows the velocity field with no fin in place, in which vectors of the

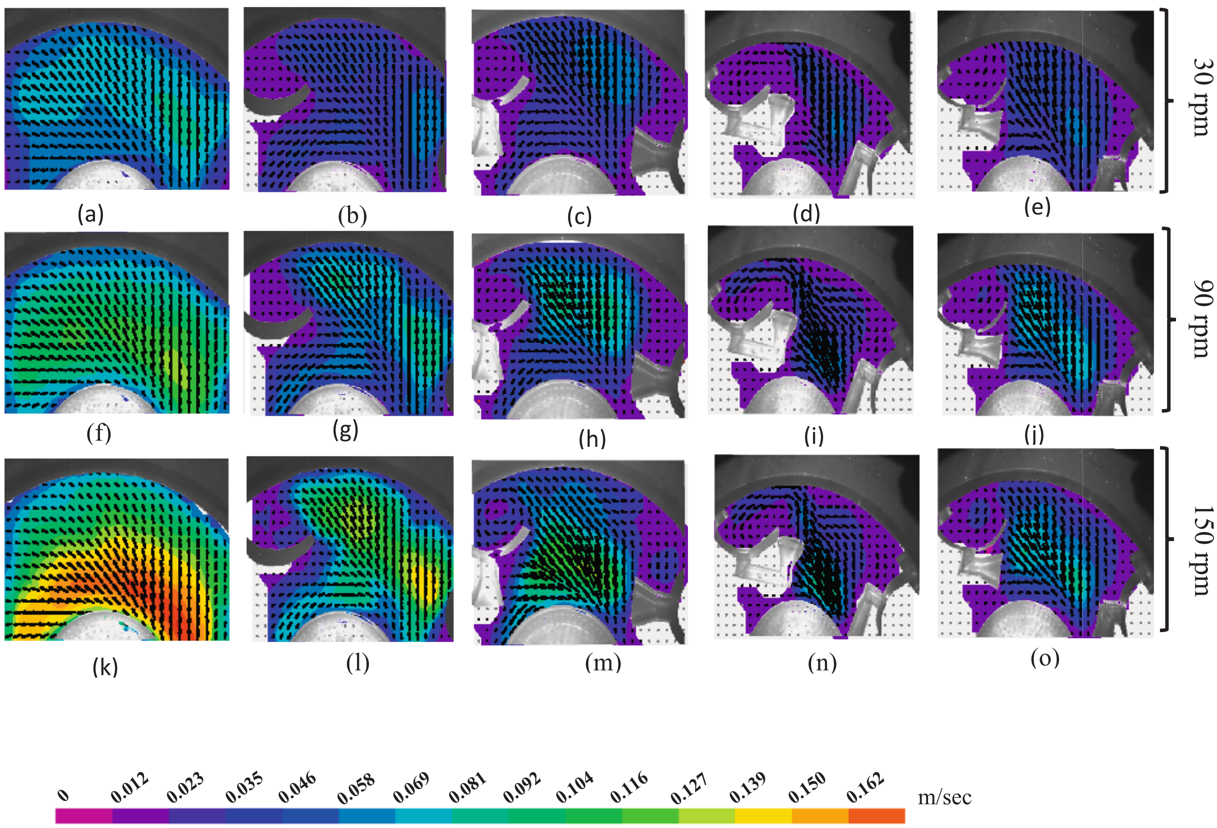

Fig. 6. Liquid-phase velocity fields measured inside the collar under single-phase conditions (no air injection). Rows (top to bottom) correspond to sparger rotation speeds of 30, 90, and 150 rpm, while columns (left to right) represent the five configurations: (a, f, k) no fin, (b, g, l) simple holes, (c, h, m) straight open channel, (d, i, n) 180° open channel, and (e, j, o) 90° open channel.

highest magnitude are observed. In contrast, as seen in Fig. 6, the lowest velocities are observed for the 90° open channel (pictorially shown in Fig. 2). The mechanism underlying the maximum dissipation of liquid momentum for 90° open channel is illustrated in Fig. 7. Water is guided by the round, curved wall of the fin toward the inlet of the open channel. A change in liquid momentum occurs first due to the change in flow direction at the 90° bend, followed by the expansion at the exit of the fin. Friction contributes to a further reduction in liquid momentum as the liquid travels through the channel and negotiates the bend, and the enlarged exit section decelerates the liquid still further. Contrary to this, for the other three open channels, the fluid loses the leasts momentum. In the case of a simple hole (Fig. 2**a**), the fluid has lost the least momentum as the flow faces the least resistance. Whereas, in the case of a straight open channel (pictorially shown as Fig. 2**b**), there is a marked increase in momentum loss as compared to a simple hole because the straight open channel contains an expansion region through which the

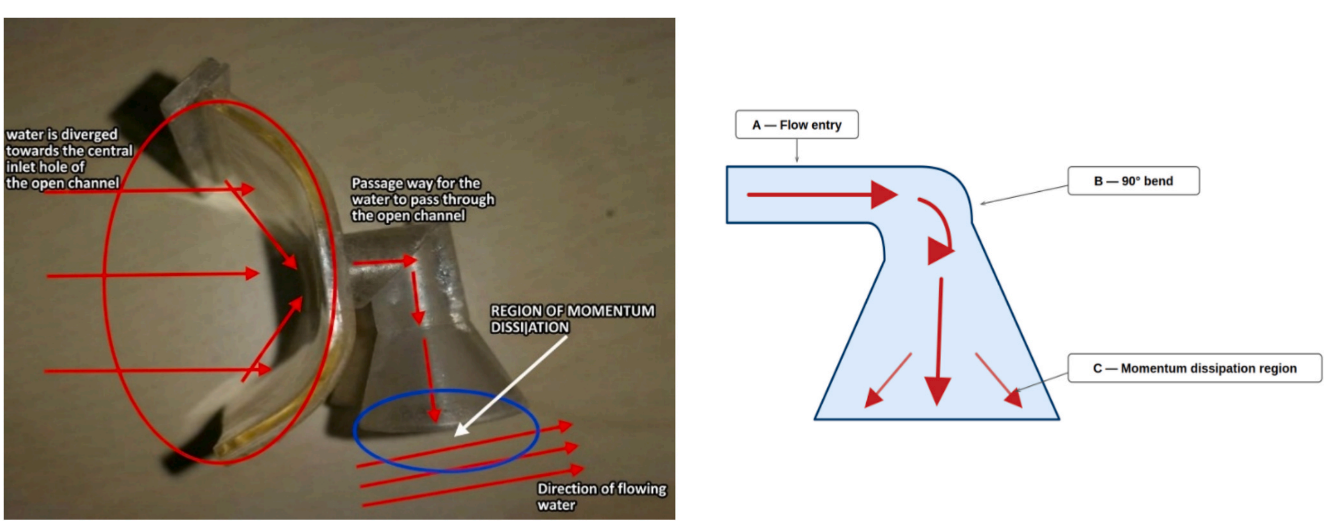

Fig. 7. Photograph of the 90° open-channel fin (left) and the corresponding schematic (right) illustrating the liquid momentum dissipation mechanism. Labels A–C identify corresponding regions in both panels: (A) flow entry (B) 90° bend, (C) momentum dissipation region where the flow spreads and decelerates. The photograph and schematic are shown from the same viewpoint to allow direct comparison of the physical geometry with the idealized flow mechanism.

liquid slows down. Whereas, both open channels bent with 90° (pictorially shown as Fig. 2**c**) and 180° (pictorially shown as Fig. 2**d**) incur much larger momentum loss for the liquid that passes through these two as compared to a simple hole and straight open channel. However, despite containing two bends, the 180° channel performs slightly less effectively than the 90° open channel in slowing down the liquid.

Although the 180° open channel appears to produce a broader low-velocity zone in Fig. 6, this visual impression does not correspond to greater momentum dissipation. The 90° geometry achieves superior performance through a single bend followed by an outlet expansion that acts as a diffuser. This configuration generates Dean-type secondary vortices and an adverse pressure gradient, converting swirl kinetic energy into static pressure and spreading the discharge uniformly. The 180° channel, by contrast, introduces two opposite bends that trigger flow separation and recirculation pockets near the inner wall. These pockets enlarge the slow region but also constrict the effective area, which accelerates a narrow high-speed streak that carries residual swirl beyond the collar. Consequently, the 90° open channel yields greater and more uniform momentum dissipation, reflected in velocity reductions of 57% inside and 64% above the collar, compared with 42% and 56%, respectively, for the 180° design.

The velocity profiles at 150 rpm inside the collar from Fig. 6 **(k-o)** are re-plotted in three dimensions in Fig. 8. Comparing the maximum velocity with no fin against those with the four fins configurations, summarized in Table 1, the velocity is reduced by 14% with the simple hole fin and 35% with the straight open channel. For the 90° and 180° bend open channels, 57% and 42% reductions in velocity are observed, respectively.

To provide a broader quantitative basis beyond the local $V_{\max}$, area-averaged velocity ($\overline{U}$) and momentum flux ($\Phi_m = \int\int \rho u^2 dA$) were evaluated over the PIV field. For single-phase flow at 150 rpm, the 90° open channel exhibited the greatest overall reduction in mean momentum flux, approximately 55% inside the collar and 63% above it, followed by 180° (41% and 54%), straight (34% and 40%), and simple-hole (17% and 28%) configurations. The 90° channel thus not only suppresses local peak velocities but also reduces the integral momentum transported through the flow cross-section, confirming its superior dissipation capability. Corresponding uncertainty bounds were determined using the combined velocity uncertainties described in Section 4.

Table 1
Maximum velocity with or without fins inside and above the collar.

Case no.	RPM	Fins/open channel	V_{max} (m/s)	
			Inside Collar	Above Collar (5 cm)
1	30 90 150		0.048 0.065 0.120	0.006 0.008 0.012
2	30 90 150		0.047 0.065 0.10	0.006 0.007 0.009
3	30 90 150		0.043 0.050 0.060	0.003 0.005 0.006
4	30 90 150		0.042 0.035 0.070	0.005 0.006 0.008
5	30 90 150	No Fin	0.065 0.10 0.17	0.009 0.012 0.014

The velocity fields presented in Fig. 8 are mean velocity fields obtained by averaging over a sufficient number of double-framed images. This averaging process ensures that the transient fluctuations are minimized, and the resulting velocity fields provide a reliable representation of the steady-state flow. To verify the accuracy of the averaging, a statistical convergence analysis was performed, confirming that the mean velocity stabilized after processing, demonstrating that the

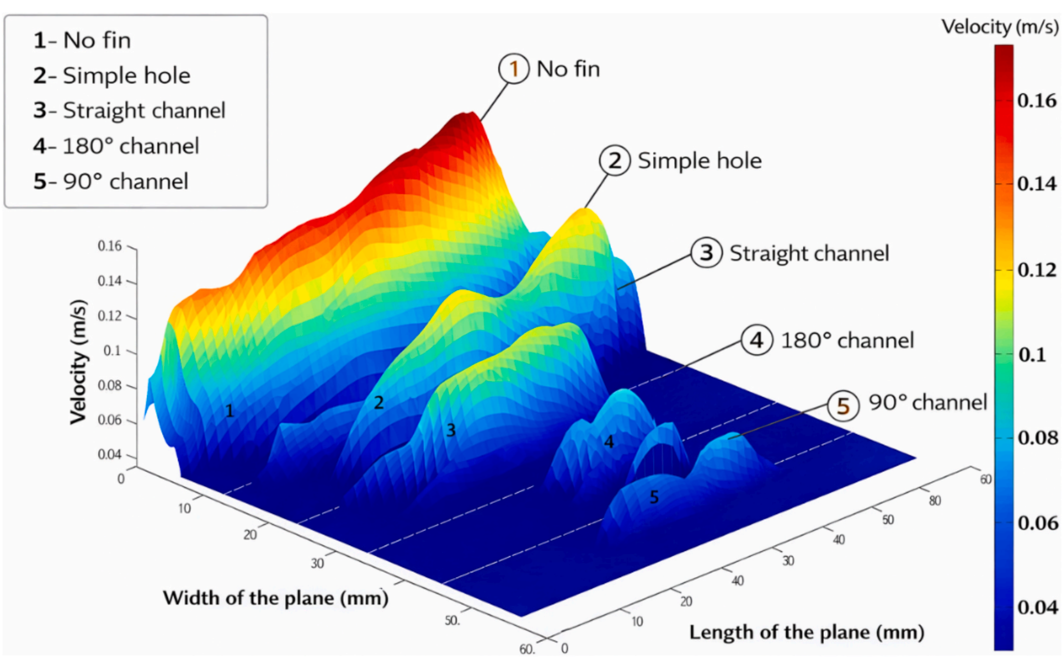

Fig. 8. Three-dimensional visualization of the liquid-phase velocity field inside the collar at 150 rpm under single-phase operation. Surface height and color indicate velocity magnitude (m/s) for the five fin configurations.

mean velocity fields are representative and robust. The mean velocity fields presented are a robust and reliable representation of the flow dynamics under the conditions studied. The focus of this research is on the overall dissipation of liquid momentum due to different fin configurations, which are well captured by the mean flow profiles. While transient or higher-order flow features may provide additional insights, the primary conclusions of the study regarding the relative performance of the different geometrical configurations in dissipating momentum are fully supported by the mean flow data. It is worth noting that, while focusing on mean flow analysis, the flow is not laminar, and the complex flow interactions induced by the rotating sparger and fin geometries suggest the presence of unsteady, turbulent features in the system. While pressure analysis could provide additional valuable insights, the current study focuses on the effects of fin geometry on momentum dissipation, which is effectively captured through the presented velocity field data.

Although the 180° open channel exhibits a broader low-velocity region in the PIV plots (Fig. 6), this does not directly indicate better momentum dissipation. The 90° configuration outperforms due to its simpler single-turn geometry, which induces Dean-type secondary vortices and an effective diffuser action at the outlet. These features redistribute azimuthal momentum more uniformly and reduce peak liquid velocities across the plane. Conversely, the 180° configuration introduces two opposing bends, generating secondary flow reversal and localized separation near the inner wall. This causes recirculation pockets and a narrowed effective flow path, resulting in a concentrated high-speed jet that transmits residual swirl beyond the collar. Consequently, the 180° geometry yields larger but less effective stagnant zones, whereas the 90° geometry achieves smoother and more uniform dissipation of liquid momentum, minimizing swirl persistence above the collar.

(b) Above the collar

A plane 5 cm above the collar was selected to observe the effectiveness of fins in the region outside the collar. Fig. 9 **(a–o)** presents the PIV plots at this plane with rotation at 30 rpm, 90 rpm, and 150 rpm. As seen in this figure, with no fin in place, there is sufficient liquid swirl above the collar as the momentum is being conveyed here due to the rotation of the sparger. However, using fins containing open channels, the liquid momentum decreases a great deal, especially in the case of both bent open channels. The 90°channel again proves again to be the most effective of the four configurations tested for dissipating liquid momentum. Although the velocity field in Fig. 9 shows a visually larger low-velocity region for the 180° open channel, quantitative PIV data confirm that the 90° channel achieves greater overall momentum dissipation. The 180° bend introduces two curvature reversals that generate separation pockets and recirculation zones, expanding the apparent "blue" area in the PIV field but simultaneously concentrating the remaining flow into a narrow high-speed jet that transmits residual swirl beyond the collar. In contrast, the 90° channel produces a single smooth bend followed by an expansion that acts as a diffuser, converting swirl kinetic energy into pressure and distributing the outflow more uniformly. This mechanism suppresses high-velocity streaks and yields a more homogeneous velocity profile above the collar. Consequently, despite the larger stagnant region observed in the 180° configuration, the 90° geometry exhibits superior momentum-dissipation efficiency.

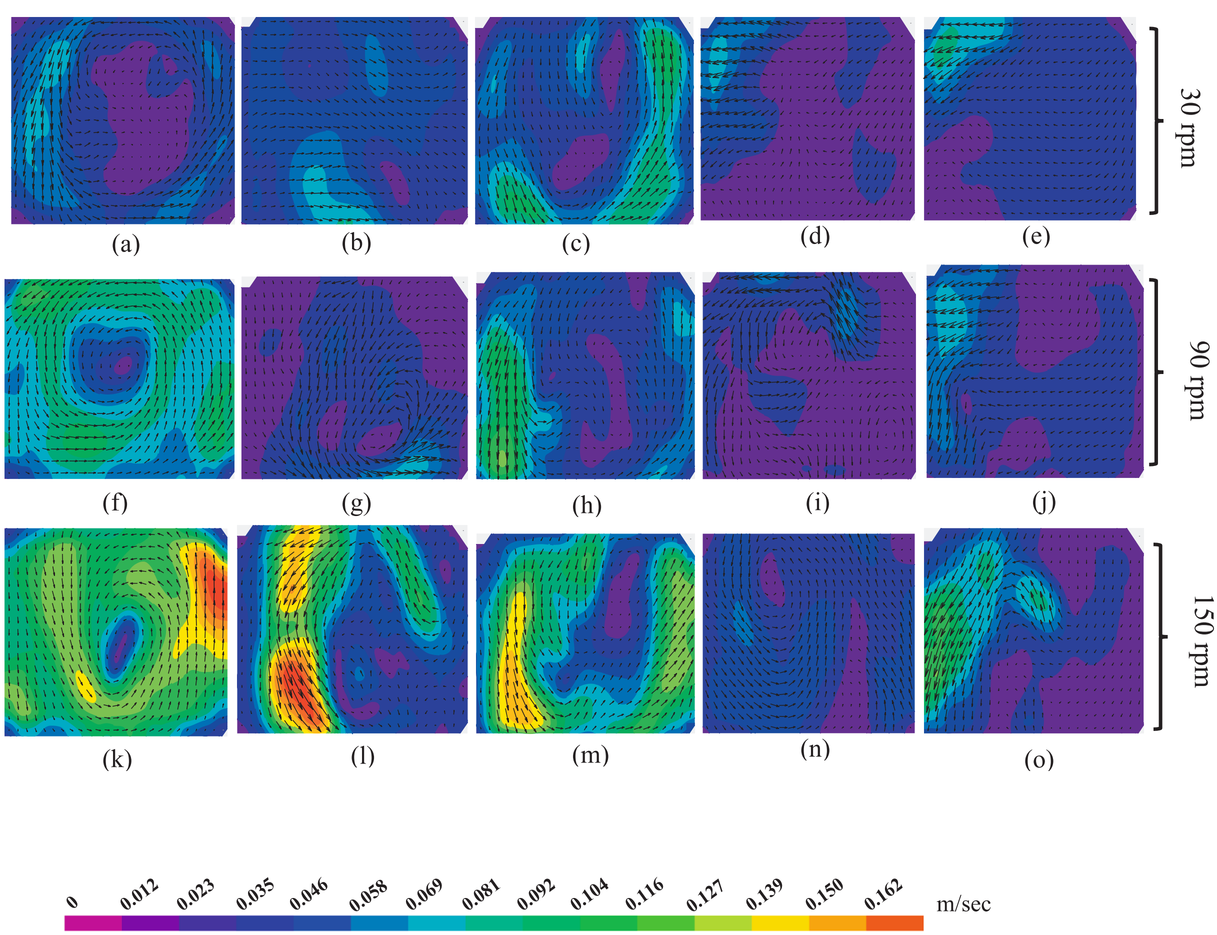

Fig. 9. Liquid phase velocity fields were measured 5 cm above the collar under single-phase conditions (no air injection). Rows (top to bottom) correspond to sparger rotation speeds of 30, 90 and 150 rpm, while columns (left to right) represent the five configurations: (a,f,k) no fin, (b, g, l) simple holes, (c, h, m) straight open channel, (d, i, n) 180° open channel and (e, j, o) 90° open channel.

The 3-D plot at 150 rpm above the collar is derived from the PIV data in Fig. 9 **(k-o)** and is presented in Fig. 10. The velocity is reduced by 29% with the simple hole fin and by41% with the straight open channel. For the 90° and 180° bent open channels, 64% and 56% reductions in velocity are observed, respectively. The remaining results are shown in tabular form in Table 1. These findings confirmed that the contrasting behavior of velocity vectors between the fin and no fin cases, observed for the horizontal plane inside the collar, also holds for the region above the collar.

3.2. Swirl flow BCR with air injection

In this case, measurements were taken at air flow rates of 0.06 g/s, 0.16 g/s, and 0.26 g/s, while the sparger rotations during these measurements were set at 30, 90, and 150 rpm. Our understanding recognizes that swirl motion can significantly impact a bubbly reactor's performance by highlighting changes in hydrodynamic parameters compared to conventional bubbly flows. However, it should be noted that increased bubble slip relative to the liquid can improve liquid dispersion. Therefore, reducing the liquid momentum generated by the sparger rotation will help maintain maximum bubble slip. Fig. 11 shows PIV measurements of the velocity field captured across a horizontal plane 5 cm above the collar in the bubble column reactor. The measurements were conducted under conditions of air injection at 0.26 g/s and a sparger rotation of 150 rpm. The figure compares velocity distributions across five configurations: no fin, simple holes, straight open channels, 90° bent open channels, and 180° bent open channels. In the no-fin case, the velocity field indicates significant liquid momentum above the collar due to the unrestrained rotational force from the sparger. High-velocity vectors are evenly distributed, showing strong swirling action without dissipation mechanisms. With simple holes, there is a slight decrease in velocity compared to the no-fin setup, as simple holes offer minimal resistance and provide little disruption to the swirling motion. Straight-open channels result in a more noticeable velocity decrease by guiding the flow and dissipating some momentum. This linear design reduces turbulence but still allows moderate swirl, leading to intermediate dissipation levels. The 90° bent open channels show the most significant reduction, with smaller, localized velocity vectors. This design redirects flow and increases resistance, efficiently dissipating energy and disrupting swirling motion. The 90° channels achieve a 44% velocity reduction relative to no fins, making them the most effective for momentum dissipation. The 180° bent open channels also lower velocities considerably but are slightly less effective than the 90° version. The additional bends may induce flow separation and recirculation, reducing efficiency, yet they still produce a 35% velocity reduction. Overall, velocity decreases as the fin geometry becomes more complex, with 90° and 180° bent channels outperforming the straight channels and simple holes. These findings demonstrate the effectiveness of fin designs in modifying hydrodynamics above the collar. The introduction of air increases liquid circulation and induces vortex shedding off rising bubbles, thus, overall liquid velocity is raised by approximately 90% compared to single-phase conditions. In this regime, fin geometry plays an even more significant role in controlling momentum transfer. The 90° open channel maintains its advantage because its single turn plus diffuser-like expansion dissipates both swirl and bubble-induced kinetic energy, which minimizes jetting and preserves bubble–liquid slip. The 180° channel still produces large recirculation pockets but also concentrates part of the flow into a faster core jet, and transmits residual swirl. Quantitatively, at 150 rpm and 0.26 g/s air flow, the 90° configuration reduces the liquid velocity by 44%, versus 35% for the 180° design, confirming that the same flow-mechanism trend holds in two-phase operation. The data underscores the importance of fin geometry in controlling momentum dissipation, which is crucial for enhancing reactor performance and reducing energy loss in industrial applications. Fig. 12 displays 3-D velocity profiles from PIV data, comparing maximum velocities with no fins and all four fin types. The velocity decreases by 11% with the simple hole fin and 22% with the straight open channel. For the 90° and 180° bent open channels, velocity reductions of 44% and 35%, respectively, were observed. Comparing the velocity fields of bubbly flow (Fig. 11a) with those obtained by simply rotating the sparger at 150 rpm without air injection (Fig. 10*k*), it reveals that bubbly flow increases the measured liquid-phase maximum velocity by approximately an **order of magnitude (≈ 13–17 ×)** compared to single-phase conditions, as seen from Tables 1 and 2. This substantial increase arises from enhanced circulation and vortex shedding caused by the bubbles. Table 2 lists maximum velocity (V_{max}) measurements above the collar during air injection for different fin configurations and rotational speeds. The data are grouped into five cases, each tested at flow rates of 0.06, 0.16, and 0.26 kg/s. It shows that increasing the number of fins and RPM generally raises Vmax values.

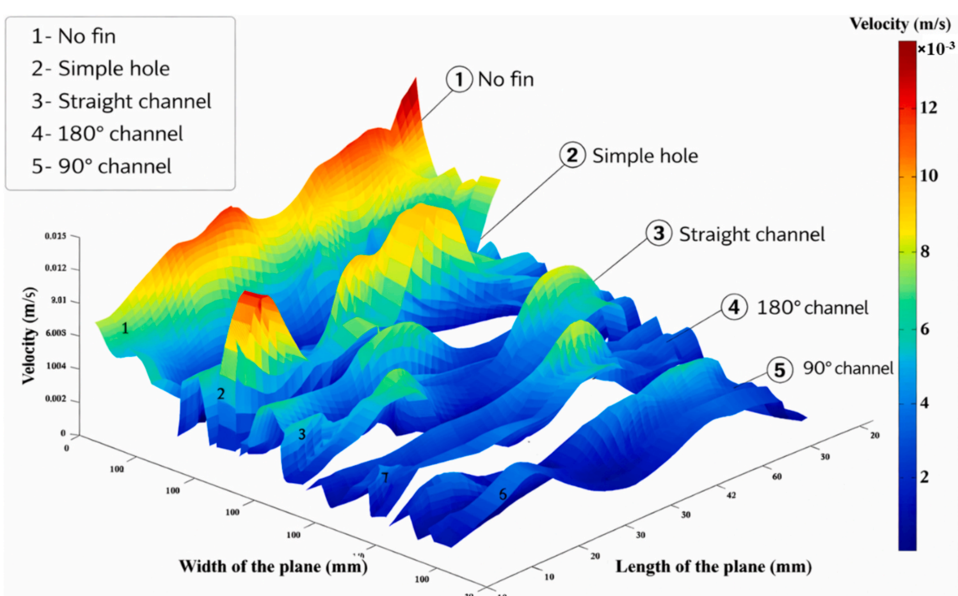

Fig. 10. Three-dimensional visualization of the liquid-phase velocity field measured 5 cm above the collar at 150 rpm under single-phase operation. Velocity magnitude is represented by surface height and color (m/s).

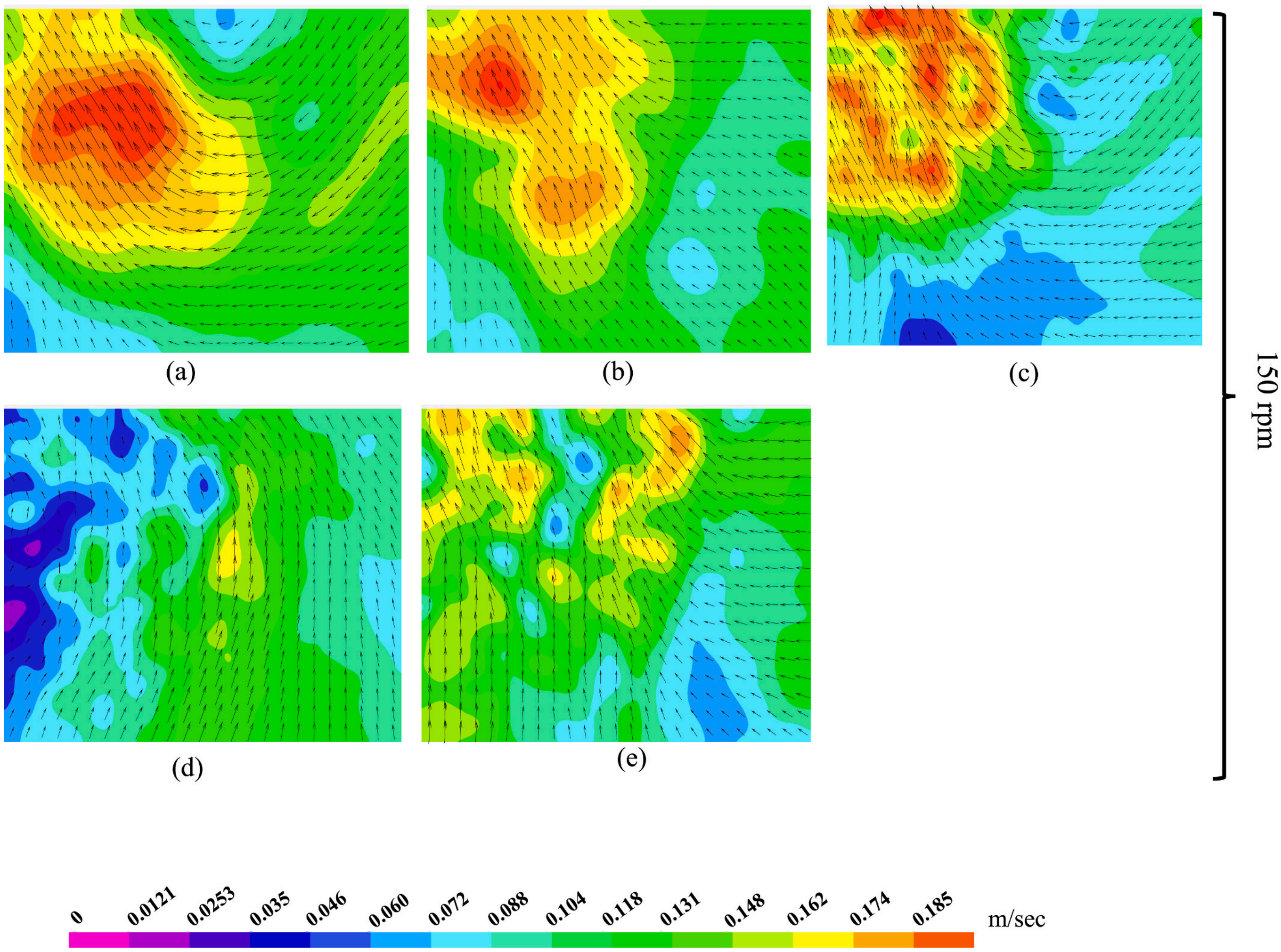

Fig. 11. PIV-measured liquid-phase velocity fields 5 cm above the collar during air–water two-phase operation. Measurements were conducted at an air flow rate of 0.26 g/s and a sparger rotation speed of 150 rpm. The figure compares (a) no fin, (b) simple holes, (c) straight channels, (d) 90° open channels, and (e) 180° open channels. Bubble regions were masked during PIV processing; only liquid velocities are shown. The 90° open channel exhibits the greatest reduction in liquid velocity, indicating superior momentum dissipation under aerated conditions.

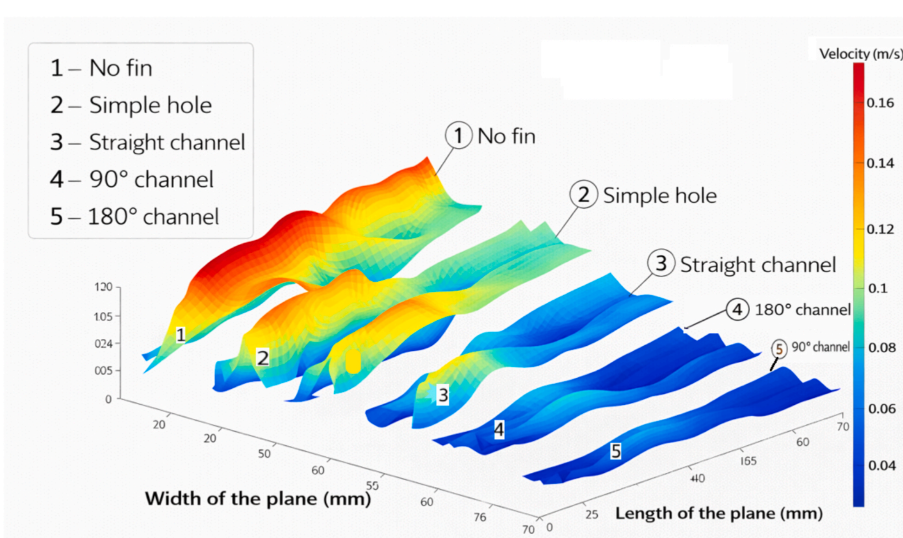

Fig. 12. Three-dimensional visualization of the liquid-phase velocity field measured 5 cm above the collar during air–water operation at 0.26 g/s and 150 rpm. Surface height and color represent velocity magnitude (m/s).

Table 2
Maximum velocity with or without fins above the collar with air injection.

Case no.	RPM	Fins/open channel	V_{max} (m/s) at flow rate 0.06 g/s	V_{max} (m/s) at flow rate 0.16 g/s	V_{max} (m/s) at flow rate 0.26 g/s
1	30 90 150		0.06 0.09 0.11	0.085 0.010 0.131	0.12 0.14 0.16
2	30 90 150		0.05 0.071 0.095	0.078 0.085 0.010	0.10 0.12 0.14
3	30 90 150		0.036 0.044 0.067	0.055 0.069 0.082	0.07 0.085 0.10
4	30 90 150		0.042 0.059 0.075	0.063 0.080 0.094	0.09 0.11 0.13
5	30 90 150	No Fin	0.095 0.113 0.135	0.11 0.134 0.159	0.13 0.155 0.18

Case 5, which has no fins, consistently exhibits the highest velocities across all flow rates and speeds, indicating that the lack of fins allows greater airflow. Conversely, cases with fins (cases 1–4) show varied results, with higher RPMs usually boosting airflow, though the specific fin geometry and placement also influence performance. This table emphasizes how fin design and operational speed impact air velocity in the system. It should be noted that only liquid-phase PIV measurements were conducted in this study; gas-phase velocities and bubble trajectories were not directly measured. Consequently, bubble slip velocity was evaluated qualitatively from differences between liquid flow fields under single- and two-phase conditions.

To verify the statistical robustness of the velocity field data, a convergence analysis was performed by progressively averaging subsets of the 50 double-frame image pairs and evaluating the corresponding mean velocity and standard error. As shown in the supplementary analysis, the mean velocity values stabilized after approximately 40 samples, and the standard error fell below 2% of the mean beyond this point. These results confirm that using 50 image pairs per condition provides statistically converged and representative mean velocity fields. Therefore, the velocity maps presented in Figs. 6, 9, and 11 can be considered reliable for quantitative comparison among fin configurations.

3.3. Contextualization using dimensionless parameters

To place the present results in a broader hydrodynamic context, the operating range was characterized using the dimensionless parameters commonly employed in studies of swirling bubble column flows. The Reynolds number, defined as

$$Re = \frac{\rho \times U \times D}{\mu}$$

based on the column inner diameter D and the mean liquid velocity U, varied from approximately 5.3×10^4 at 30 rpm to 2.1×10^5 at 150 rpm. These values lie within the transitional-to-turbulent regime typical of laboratory-scale bubble column reactors. The influence of rotation was characterized by the Froude number,

$$Fr = \frac{\Omega^2 \times R}{g}$$

which represents the ratio of centrifugal to gravitational forces ranged from 0.18 to 0.52 over the investigated rotation speeds. The rotational velocity ratio $\Omega R/U$ varied between 0.35 and 0.6, indicating moderate swirl intensities consistent with practical swirl-assisted bubble column operation.

It is important to emphasize that these parameters span less than one order of magnitude, and the present experiments were conducted at a single geometric scale. The data, therefore, do not constitute a scaling or scale-up analysis and cannot be used to infer scale-independent behavior. Their purpose here is to (i) document the flow regime in which the measurements were obtained, (ii) enable comparison with other swirling bubble column studies operating in similar regimes, and (iii) provide a reference framework for future investigations across wider parameter ranges. Within the investigated ranges of Re, Fr, and $\Omega R/U$, the relative ranking of the four fin geometries and in particular the consistently superior performance of the 90° open channel was preserved at all tested operating conditions. Whether this ranking persists at substantially different Reynolds and Froude numbers, or at larger geometric scales, is a question that requires dedicated multi-scale experiments and is identified here as a direction for future work.

4. Uncertainty analysis

4.1. Measurement model

All liquid-phase velocities were derived from particle image displacements measured over a known inter-frame time and mapped to physical (object space) coordinates through the spatial calibration of the imaging system:

$$u = \frac{M\Delta x}{\Delta t} \tag{4}$$

where M is the image-to-object scale factor (m/pixel), Δx is the measured particle displacement (pixels), and Δt is the inter-frame time (s).

The velocity fields reported in this study were obtained from double-framed PIV images captured by a 1600 × 1200 pixel CCD camera and illuminated by a dual-pulsed Nd:YAG laser at 532 nm. For each operating condition, 50 image pairs were acquired. Cross-correlation was performed using a 64 × 64 pixel interrogation window with 50% overlap, followed by outlier validation and spatial filtering (section 2.2).

4.2. Random (Type-A) uncertainty

At each measurement location, instantaneous velocities from the *N* = 50 image pairs were ensemble-averaged to obtain the mean velocity $\overline{u}$. The sample standard deviation and the standard error of the mean were computed as

$$\varepsilon_u = \sqrt{\frac{1}{N-1}\sum_{i=1}^{N}(u_i-\overline{u})^2},\ \mathrm{SE}(\overline{u}) = \frac{s_u}{\sqrt{N}},\ N = 50 \tag{5}$$

The 95% confidence interval of the mean velocity is given by $\overline{u} \pm 1.96\mathrm{SE}(\overline{u})$. A statistical convergence assessment confirmed that $\overline{u}$ stabilized within the ensemble of 50 image pairs (Section 3.2), indicating that the type-A contribution is small relative to the geometric effects compared in Section 3.

4.3. Systematic (Type-B) uncertainty

The combined relative standard uncertainty of a single velocity vector is given by

$$\left(\frac{U_x}{u}\right)^2 = \left(\frac{U_{\Delta x}}{\Delta x}\right)^2 + \left(\frac{U_M}{M}\right)^2 + \left(\frac{U_{\Delta t}}{\Delta t}\right)^2 + (\text{other bias terms})^2 \quad (6)$$

Where the final summation collects the remaining bias contributions discussed below. The principal sources of systematic uncertainty are:

Image-displacement uncertainty ($U_{\Delta\sigma}$). Determined by the cross-correlation peak locking error and the local signal-to-noise ratio. The 64 × 64 pixel interrogation windows with 50% overlap, and the neighborhood-validation filter applied during post-processing minimizes this term.

Spatial-scale uncertainty (U_M). Calibration was performed using known geometric dimensions (collar ID = 0.20 m; fixed measurement planes inside the collar and 5 cm above its top edge. Optical distortion arising from the column curvature was minimized by surrounding the cylindrical column with a rectangular outer box filled with the same working fluid and constructed from the same material.

Timing uncertainty ($U_{\Delta t}$). The inter-frame interval ($\Delta t = 750$ µs) was set by the synchronized laser camera electronics and contributes negligibly compared with $U_{\Delta x}$ and U_M.

Tracer-particle fidelity. Hollow glass spheres (mean diameter 10 µm; density ≈1.1 g/cm^3) yielded Stokes numbers ranging from St = 1.38 × 10^{-5} at the highest measured velocity ($u = 0.18$ m/s) to St = 7.64 × 10^{-7} at the lowest ($u = 0.01$ m/s), confirming negligible velocity lag between tracers and the surrounding liquid.

Out-of-plane motion. Two-dimensional PIV with a thin laser sheet is sensitive to out-of-plane particle excursions, which can degrade correlation quality. The masking and validation steps illustrated in Fig. 5 minimize the propagation of this bias into the final vector fields.

Auxiliary Instrumentation. The thermal mass flow meter has a stated accuracy of ±1.5% of full scale. Sparger rotation speeds (30, 90, 150 rpm) were set by a calibrated variable speed motor controller; the corresponding tachometer uncertainty is negligible relative to the velocity differences being compared between fin configurations.

4.4. Combined uncertainty of velocity

For a single vector, the combined standard uncertainty is obtained by the quadrature combination of the dominant contributions:

$$U_u = u\sqrt{\left(\frac{U_{\Delta x}}{\Delta x}\right)^2 + \left(\frac{U_M}{M}\right)^2 + \left(\frac{U_{\Delta t}}{\Delta t}\right)^2} \quad (7)$$

For spatial statistics such as the maximum plane velocity $V_{max.}$, the systematic and random contributions are combined as

$$U_{V_{x-x}} = \sqrt{U^2_{u,x>x} + \left(1.96\frac{s_{V_{n-a}}}{\sqrt{N}}\right)^2} \quad (8)$$

4.5. Uncertainty of the momentum dissipation ratio

The reported momentum-dissipation ratio is defined as

$$R = 1 - \frac{V_{fin}}{V_{nolin}} \quad (9)$$

Where V_{fin} and V_{nofin} are the maximum (or area-averaged) velocities measured with and without the fin in place, respectively. Propagating the uncertainties of the two velocities gives

$$U_R = \sqrt{\left(\frac{U_{V_{in}}}{V_{min}}\right)^2 + \left(\frac{V_{fin}U_{V_{inf}}}{V^2_{in}\mathrm{fin}_{in}}\right)^2} \quad (10)$$

and the corresponding 95% confidence interval is $R \pm 1.96U_R$. These expressions were applied consistently to both the single-phase data (Figs. 6-10, Table 1) and the two-phase data (Figs. 11-12, Table 2).

4.6. Experimental Controls and Mitigations

Several measures were implemented to minimize systematic bias:

- Optical correction. A rectangular, water-filled outer box constructed from the same Perspex material as the column eliminated curvature-induced refraction at the cylindrical wall.
- Seeding & masking. Bubble regions were masked prior to cross-correlation, and spurious vectors were removed using neighborhood validation (Section 2.2).
- Plane alignment. Both measurement planes were fixed to reproducible heights (inside the collar and 5 cm above its top edge) for all experiments.

Combining the contributions discussed above, the overall relative uncertainty in measured liquid phase velocities is estimated to be below ±3%. This is substantially smaller than the 15 −25% velocity differences observed between fin configurations, confirming that the reported trends and ranking of geometries are statistically significant. The same propagated uncertainties were applied to the integral momentum flux and area averaged velocity metrics introduced in Section 3.1, supporting the conclusion that the 90° open channel produces the greatest reduction in liquid momentum across all tested operating conditions.

5. Conclusions

This study experimentally investigated the hydrodynamics of a bubble column reactor with swirl gas injection, focusing on the effects of fin geometries on liquid momentum dissipation under single- and two-phase conditions. PIV measurements showed that the 90° bent open channel achieved the highest momentum dissipation, reducing liquid velocity by 57% inside the collar and 64% above it, followed by the 180° bent open channel with reductions of 42% and 56%, respectively. The straight channels and simple holes produced comparatively lower velocity reductions of 35% and 14% inside the collar and 41% and 29% above it, respectively. Under aerated conditions, swirl gas injection increased the liquid-phase velocity by approximately 90% compared to non-swirl operation, while the relative effectiveness of the fin geometries remained consistent.

Although heat and mass transfer were not directly measured in this study, the observed enhancement in mixing and modification of the liquid velocity field suggests that improved phase interaction may be achievable using the proposed momentum dissipation designs. The results indicate that controlled dissipation of swirl-induced liquid momentum could be beneficial for reactor operation in applications requiring stable hydrodynamics and efficient phase interaction. Although potential applications such as effluent treatment and biofuel production were not explored in detail here, the present findings provide a hydrodynamic basis for future investigations. Further studies incorporating direct measurements of mass transfer and process performance are needed to validate these implications and to assess the practical significance of the proposed designs.

CRediT authorship contribution statement

Ahmad Salam Farooqi: Writing – original draft, Investigation, Formal analysis. **Khairuddin Sanaullah:** Supervision, Methodology, Funding acquisition. **Mohamed A. Kotb:** Writing – review & editing. **Nicholas J. Watson:** Writing – review & editing, Supervision. **Atia E. Khalifa:** Writing – review & editing, Resources. **Shahid Rasul:** Writing – review & editing. **Medhat A. Nemitallah:** Visualization, Resources.

Declaration of competing interest

The authors declare that they have no known competing financial interests or personal relationships that could have appeared to influence the work reported in this paper.

Acknowledgment

The authors gratefully acknowledge the support received from the Newton Research Collaboration Programme (NRCP) between Universiti Malaysia Sarawak, Malaysia and University of Nottingham, U.K (Grant No. GL/F02/NEWTON/2016); Centre of Automotive Research and Electrical Mobility (CAREM), Universiti Teknologi PETRONAS, Malaysia; and the Deanship of Research at King Fahd University of Petroleum and Minerals (KFUPM) through Project No. POC26101.

Data availability

Data will be made available on request.

References

[1] M.T. Dhotre, K. Ekambara, J.B. Joshi, CFD simulation of sparger design and height to diameter ratio on gas hold-up profiles in bubble column reactors, Exp. Therm Fluid Sci. 28 (2004) 407–421, https://doi.org/10.1016/j.expthermflusci.2003.06.001.

[2] N. Kantarci, F. Borak, K.O. Ulgen, Bubble column reactors, Process Biochem. 40 (2005) 2263–2283, https://doi.org/10.1016/j.procbio.2004.10.004.

[3] H. Jin, Y. Lian, L. Qin, S. Yang, G. He, Z. Guo, Parameters measurement of hydrodynamics and CFD simulation in multi-stage bubble columns, Can. J. Chem. Eng. 92 (2014) 1444–1454, https://doi.org/10.1002/cjce.22005.

[4] R. Krishna, M.I. Urseanu, A.J. Dreher, Gas hold-up in bubble columns: Influence of alcohol addition versus operation at elevated pressures, Chem. Eng. Process. 39 (2000) 371–378, https://doi.org/10.1016/S0255-2701(00)00093-3.

[5] M. Kotb, A. Khalifa, S.M. Alawad, Experimental evaluation of membrane distillation and bubble column dehumidifier bank desalination system for Balancing productivity and energy efficiency, Appl. Therm. Eng. 272 (2025) 126397, https://doi.org/10.1016/j.applthermaleng.2025.126397.

[6] M. Kotb, A. Khalifa, Novel vacuum membrane distillation operated by air ejector and bubble column dehumidifier for sustainable water desalination-energetic, exergetic, and economic analysis, Sep. Purif. Technol. 371 (2025) 133368, https://doi.org/10.1016/j.seppur.2025.133368.

[7] M. Irani, M.A. Khodagholi, Investigation of bubble column hydrodynamics using CFD simulation (2D and 3D) and experimental validation, Pet. Coal 53 (2011) 146–158.

[8] Z. Zhou, Q. Yuan, X. Jia, W. Feng, J. Wen, Experimental study and CFD simulation of mass transfercharacteristics of a gas-induced pulsating flow bubble column, Chem. Biochem. Eng. Q. 27 (2013) 167–175.

[9] M. Kotb, A. Khalifa, A. Hussein, S.M. Alawad, M. Antar, Performance and exergy analysis of vacuum-assisted sweeping air membrane distillation and bubble column dehumidifier, Appl. Therm. Eng. 245 (2024) 122800, https://doi.org/10.1016/j.applthermaleng.2024.122800.

[10] S.M. Alawad, O. Shamet, D. Lawal, A.E. Khalifa, M. Kotb, The optimum location of vapor compressor in multistage vacuum membrane distillation system, Therm. Sci. Eng. Prog. 56 (2024) 103089, https://doi.org/10.1016/j.tsep.2024.103089.

[11] R.F. Mudde, Gravity-driven bubbly flows, Annu. Rev. Fluid Mech. 37 (2005) 393–423, https://doi.org/10.1146/annurev.fluid.37.061903.175803.

[12] B.N. Thorat, Effect of sparger design and height to diameter ratio on fractional gas hold-up in bubble columns, Chem. Eng. Res. Des. 76 (1998) 823–834, https://doi.org/10.1205/026387698525577.

[13] M. Kotb, M. Abido, A. Khalifa, Single and multi-objective optimization of sweeping gas membrane distillation with double-stage bubble column dehumidifier, Sep. Purif. Technol. 359 (2025) 130481, https://doi.org/10.1016/j.seppur.2024.130481.

[14] A.V. Kulkarni, J.B. Joshi, Design and selection of sparger for bubble column reactor. Part I: Performance of different spargers, Chem. Eng. Res. Des. 89 (2011) 1972–1985, https://doi.org/10.1016/j.cherd.2011.01.004.

[15] A.A. Kulkarni, J.B. Joshi, Bubble formation and bubble rise velocity in gas-liquid systems: a review, Ind. Eng. Chem. Res. 44 (2005) 5873–5931, https://doi.org/10.1021/ie049131p.

[16] A.A. Mouza, G.K. Dalakoglou, S.V. Paras, Effect of liquid properties on the performance of bubble column reactors with fine pore spargers, Chem. Eng. Sci. 60 (2005) 1465–1475, https://doi.org/10.1016/j.ces.2004.10.013.

[17] X. Luo, D.J. Lee, R. Lau, G. Yang, L.S. Fan, Maximum stable bubble size and gas holdup in high-pressure slurry bubble columns, AIChE J 45 (1999) 665–680, https://doi.org/10.1002/aic.690450402.

[18] A. Schumpe, G. Grund, The gas disengagement technique for studying gas holdup structure in bubble columns, Can. J. Chem. Eng. 64 (1986) 891–896, https://doi.org/10.1002/cjce.5450640602.

[19] S. Martemianov, V.L. Okulov, On heat transfer enhancement in swirl pipe flows, Int. J. Heat Mass Transf. 47 (2004) 2379–2393, https://doi.org/10.1016/j.ijheatmasstransfer.2003.11.005.

[20] A. Hamdani, T. Ihara, N. Tsuzuki, H. Kikura, Experimental study of bubbly swirling flow in a vertical tube using ultrasonic velocity profiler (UVP) and wire mesh sensor (WMS), J. Mech. Sci. Technol. 30 (2016) 3897–3905, https://doi.org/10.1007/s12206-016-0801-6.

[21] M.V. Holloway, H.L. McClusky, D.E. Beasley, M.E. Conner, The effect of support grid features on local, single-phase heat transfer measurements in rod bundles, J. Heat Transfer 126 (2004) 43–53, https://doi.org/10.1115/1.1643091.

[22] J.Z. Kovacevic, M.N. Pantzali, K. Niyogi, N.G. Deen, G.J. Heynderickx, G.B. Marin, Solids velocity fields in a cold-flow gas-solid vortex reactor, Chem. Eng. Sci. 123 (2015) 220–230, https://doi.org/10.1016/j.ces.2014.10.020.

[23] W. Liu, B. Bai, Swirl decay in the gas-liquid two-phase swirling flow inside a circular straight pipe, Exp. Therm Fluid Sci. 68 (2015) 187–195, https://doi.org/10.1016/j.expthermflusci.2015.04.018.

[24] B. Sreenivasan, V.R. Raghavan, Hydrodynamics of a swirling fluidised bed, Chem. Eng. Process. 41 (2002) 99–106, https://doi.org/10.1016/S0255-2701(00)00155-0.

[25] R. Cazan, C.K. Aidun, Experimental investigation of the swirling flow and the helical vortices induced by a twisted tape inside a circular pipe, Phys. Fluids 21 (2009), https://doi.org/10.1063/1.3085699.

[26] M.A. Kotb, A.E. Khalifa, A novel vacuum membrane distillation system with water ejector: Performance assessment and optimization, Energ. Conver. Manage. 343 (2025) 120239, https://doi.org/10.1016/j.enconman.2025.120239.

[27] A. Mohammadpour, M.A. Akhavan-Behabadi, M. Ebrahimzadeh, P. Hanafizadeh, M. Raisee, Experimental determination of void fraction in surface aeration using image processing technique, J. Mech. Sci. Technol. 29 (2015) 2391–2400, https://doi.org/10.1007/s12206-015-0530-2.

[28] M. Sivaiah, R. Parmar, S.K. Majumder, A.E. Setup, Hydrodynamics of Bubbly Flow in a Modified Reactor 6 (2012) 82–85.

[29] K. Shanmugam, K. Saravanan, V. Ramamoorthy, R. Balasubramani, Hydrodynamic Studies in Stirred Bubble Column (2008) 113–118.

[30] G.P. Lucas, R. Mishra, Measurement of bubble velocity components in a swirling gas-liquid pipe flow using a local four-sensor conductance probe, Meas. Sci. Technol. 16 (2005) 749–758, https://doi.org/10.1088/0957-0233/16/3/018.

[31] M. Wang, G. Lucas, Y. Dai, N. Panayotopoulos, R.A. Williams, Visualisation of bubbly velocity distribution in a swirling flow using Electrical Resistance Tomography, Part. Part. Syst. Char. 23 (2006) 321–329, https://doi.org/10.1002/ppsc.200601063.

[32] M. Shoukri, I. Hassan, I. Gerges, Diameter Vertical Pipes 81 (2003) 205–211.

[33] A. Melling, Tracer particles and seeding for particle image velocimetry, Meas. Sci. Technol. 8 (1997) 1406–1416, https://doi.org/10.1088/0957-0233/8/12/005.

[34] R. Lindken, L. Gui, W. Merzkirch, Velocity measurements in multiphase flow by means of particle image velocimetry, Chem. Eng. Technol. 22 (1999) 202–206, https://doi.org/10.1002/(SICI)1521-4125(199903)22:3<202::AID-CEAT202>3.0.CO;2-K.

[35] R.J. Adrian, Twenty years of particle image velocimetry, Exp. Fluids 39 (2005) 159–169, https://doi.org/10.1007/s00348-005-0991-7.

[36] R.J. Adrian, Scattering particle characteristics and their effect on pulsed laser measurements of fluid flow: speckle velocimetry vs particle image velocimetry, Appl. Opt. 23 (1984) 1690, https://doi.org/10.1364/ao.23.001690.

[37] T.R. Oakley, E. Loth, R.J. Adrian, A two-phase cinematic piv method for bubbly flows, Journal of Fluids Engineering, Transactions of the ASME 119 (1997) 707–712, https://doi.org/10.1115/1.2819302.

[38] E. Delnoij, J. Westerweel, N.G. Deen, J.A.M. Kuipers, W.P.M. Van Swaaij, Ensemble correlation PIV applied to bubble plumes rising in a bubble column, Chem. Eng. Sci. 54 (1999) 5159–5171, https://doi.org/10.1016/S0009-2509(99)00233-X.

[39] F. Pereira, M. Gharib, D. Dabiri, D. Modarress, Defocusing digital particle image velocimetry: a 3-component 3-dimensional DPIV measurement technique. Application to bubbly flows, Exp. Fluids 29 (2000), https://doi.org/10.1007/s003480070010.

[40] E. Delnoij, J.A.M. Kuipers, W.P.M. Van Swaaij, J. Westerweel, Measurement of gas-liquid two-phase flow in bubble columns using ensemble correlation PIV, Chem. Eng. Sci. 55 (2000) 3385–3395, https://doi.org/10.1016/S0009-2509(99)00595-3.

[41] Z. Liu, Y. Zheng, PIV study of bubble rising behavior, Powder Technol. 168 (2006) 10–20, https://doi.org/10.1016/j.powtec.2006.05.020.

[42] S.W. Street, Using Particle Image Velocimetry (Piv) 228 (1999) 1–8.

[43] D. Bröder, M. Sommerfeld, Planar shadow image velocimetry for the analysis of the hydrodynamics in bubbly flows, Meas. Sci. Technol. 18 (2007) 2513–2528, https://doi.org/10.1088/0957-0233/18/8/028.

[44] A.A. Araoye, W.H. Ahmed, S.A. Al, O. Bamidele, H.M. Badr, I.H. Alsurakji, Characterizing drift velocity for two-phase flow using particle image velocimetry, Advances in Fluid Mechanics XI 1 (2016) 87–97, https://doi.org/10.2495/afm160081.

[45] A. Demong, K. Sanaullah, A. Khan, A CFD study of swirl effect on hydrodynamics in a gas-liquid bubbly flow reactor, ARPN Journal of Engineering and Applied Sciences 12 (2017) 3165–3168.